J Appl Electrochem (2011) 41:773–785
DOI 10.1007/s10800-011-0295-y

ORIGINAL PAPER

Reducing the energy cost of protective anodizing

M. Curioni · P. Skeldon · J. Ferguson · G. E. Thompson

Received: 28 February 2011 / Accepted: 19 March 2011 / Published online: 1 April 2011

Abstract Minimizing the carbon footprint of electrochemical processes is an emerging challenge for electrochemists and engineers. Here, a knowledge-based methodology for development of protective anodizing cycles for aluminium alloys, enabling simultaneous tuning of electrolyte concentration, composition, temperature and process time for reduced energy consumption is presented. In order to achieve the anticorrosion properties, the morphology of the porous anodic oxides is optimized by applying advanced potential-time regimes and additions of environmentally, friendly corrosion inhibitors to the anodizing electrolyte to provide additional active protection. The anticorrosion performance of the porous anodic oxides is assessed rapidly by electrochemical noise analysis, with the electrochemical data validated by optical and electron-optical observations.

Keywords Aluminium alloy · Anodic films · Oxide coatings · Corrosion protection

1 Introduction

Maximizing energy efficiency in industrial processes has the advantage of reducing costs and minimizing the carbon footprint. Energy efficient solutions, however, must provide acceptable or enhanced performance in order to be commercially viable. Anodizing of aluminium alloys is environmentally costly due to the electrical energy consumption required for electrochemical oxidation and for the control of electrolyte temperature. While abundant data are available in the literature regarding the electrochemical efficiency of porous anodic oxide growth, defined as the ratio between the oxide thickness formed and the charge passed, typically close to 60% for acidic electrolytes [1–3], little attention has been paid to the energy efficiency, defined as the ratio between the oxide thickness formed and the electrical energy consumed. For a given current density and a given electrochemical efficiency, the energy efficiency may differ significantly, depending on electrolyte composition, concentration and temperature. For anodizing at constant current (galvanostatic), electrolyte composition, concentration and temperature determine the anodizing potential and, similarly, they determine the value of current for anodizing at constant potential (potentiostatic). Since the energy consumption can be calculated by integrating over time the product of the anodizing potential and anodizing current, independently of the choice of galvanostatic or potentiostatic conditions, electrolytes requiring higher potentials for a given current density produce porous anodic oxides at reduced energy efficiency. A typical sulphuric–tartaric process (TSA) that is the present standard for protection of aerospace components in Europe, [4–9] produces a total oxide thickness of $\sim$3–5 μm, depending on the alloy, obtained by anodizing with a voltage ramp from the open circuit potential to 14 V over 5 min and subsequent potentiostatic anodizing at 14 V for 20 min in 0.4 M H_2SO_4 with the addition of 80 g L^{-1} tartaric acid at 37 °C. For this process, a current density of $\sim$8–12 mA cm^{-2}, depending on the alloy, is passed, resulting in an energy consumption of $\sim$0.35–0.40 KW h m^{-2}. Considering the variety of possible electrolyte temperature-potential conditions available and the relatively long times required for anticorrosion performance

M. Curioni (✉) · P. Skeldon · G. E. Thompson
Corrosion and Protection Centre, School of Materials,
The University of Manchester, M13 9PL Manchester, UK
e-mail: Michele.Curioni@manchester.ac.uk

J. Ferguson
Airbus Operations Ltd, New Filton House, Filton,
Bristol BS99 7AR, UK

validation, i.e. by salt spray test (SST), it is difficult to perform systematic studies to identify the optimum process parameters for corrosion resistance and energy saving.

Recent fundamental research on the anodizing behaviour of practical alloys [10], using potentiodynamic anodizing (PDA), has characterized the behaviour in various electrolytes [8, 10]. It was revealed that, for a given electrolyte, each alloy produces a "fingerprint" current response, providing information on the current/potential relationship, the potentials for oxidation of second phase material and the maximum potential prior to localized oxide growth or burning. The minimum potential necessary for the complete oxidation of second phase material present on the alloy surface is of particular interest, since the presence of residual second phase particles on the alloy surface is associated with enhanced cathodic activity and, thus, it is detrimental to the anticorrosion performance [11]. For a given alloy, PDA has also enabled ready evaluation of the effects of specific electrolyte additions on the anodizing current density and on the oxidation behaviour of intermetallics particles [8, 12–14].

Further, the anticorrosion properties provided by the porous anodic oxide depend significantly on the anodizing potential [11, 15]. Anodic oxides generated at reduced potential display finer pores compared with oxides generated at increased potential [10, 16, 17]. Finer pores restrict access of the environment to the alloy and are capable of self-sealing by partial hydration of the alumina [11]. However, at sufficiently low anodizing potentials, second phase material present at the alloy surface may not completely oxidize, leaving residual cathodic sites at the filmed alloy surface [10, 11], with detrimental consequences on the anticorrosion performance. Therefore, to achieve optimum performance, the anodizing potential should be minimized to control the pore size, but maintained above the potential of oxidation of second phase material [11]. This route alone can improve performance and reduce energy consumption, but it is not practically employed in industrial cycles because fine pores may hinder adhesion between the oxide and polymeric adhesive primers [15]. In addition, while maintaining constant all the anodizing parameters, a reduction in the anodizing potential produces an exponential decrease in the anodizing current and, consequently, the oxide growth rate [11, 15]. Thus, the reduction of the anodizing potential alone is industrially unacceptable due to the longer times required to generate the appropriate oxide thickness.

Due to the relatively high number of anodizing parameters that can be tuned during the development of new anodizing cycles, care must be taken on the selection of a corrosion testing procedure that provides rapid highlight of the most effective routes towards improvement of protective performance, but can still be considered reliable in forecasting the real-life behaviour. SST is generally accepted as a validation procedure but it is time consuming and provides little fundamental information on the process of corrosion initiation and propagation. For this reason, it should be used more for validation of a new, well-tuned, tentative cycle rather than during the development stage. Traditional electrochemical techniques provide little information on the long term behaviour; thus, DC techniques are not always appropriate due to the large polarization applied to the corroding surface. Electrochemical impedance spectroscopy (EIS) partially overcomes this issue by applying a low amplitude sinusoidal potential perturbation. However, due to the capacitive behaviour of the oxide forming the barrier layer beneath the pores, EIS is very effective in evaluating the geometrical properties of the oxide, i.e. the barrier layer thickness, by probing the surface with a high frequency signal [18, 19]. Conversely, often EIS precision suffers from non stationarities due to corrosion events when probing the anodized surface with the low frequency signal. The latter arises from the extended duration of potential-current transients characteristic of the metal-oxide system during corrosion, often producing noisy impedance spectra at low frequencies [20]. In this study, the anticorrosion performance of similar cycles (but with different energy consumption) has been assessed by electrochemical noise analysis and optical and electron-optical observation, and subsequently compared with the current anodizing cycle that is generally adopted by the European aerospace industry [4, 6, 8, 9]. The acquisition of the electrochemical potential and current noise generated by two identical corroding specimens does not involve the application of an external potential or current; thus, no significant perturbation to the corrosion process is generated. For this reason, electrochemical noise data acquisition can be continued for long times with no interruptions, and suitable data analysis may provide information on the time evolution of the degradation process.

In this study, the available knowledge on anodizing has been exploited to tune (i) the concentration of the primary electrolyte component, sulphuric acid, (ii) the electrolyte temperature and (iii) the anodizing potential, to implement a new type of anodizing cycle. In addition to the modified temperature, sulphuric acid concentration and potential-time regime, the anodizing electrolyte has been further tuned by addition of cerium nitrate to provide extended active corrosion protection. Cerium-based compound are environmentally acceptable corrosion inhibitors, thanks to their low toxicity [21]. On practical aluminium alloys, cerium derivatives act as cathodic inhibitors and, after corrosion testing, are found predominantly close to cathodic second phase material in the form of a protective deposit [20, 22–24]. Thus, the simultaneous optimization of the process

parameters, porous anodic oxide morphology and the addition to the anodizing electrolyte of cerium nitrate as active corrosion inhibitor, enables reduction of the energy consumption maintaining a satisfactory corrosion resistance.

2 Experimental

Anodizing was undertaken on AA2024T3 aluminium alloy. Individual specimens were degreased in acetone, etched for 30 s in 100 g L^{-1} NaOH at 60 °C, desmutted for 30 s in 30 vol.% HNO_3 at room temperature, rinsed in deionised water and air dried in a cold air stream. A three-electrode cell was used, with the specimen as the working electrode, a saturated calomel reference electrode and an aluminium cathode. A Modulab potentiostat was employed to apply the potential and for data acquisition. The details of the anodizing cycles are presented in Table 1. After anodizing, the specimens were rinsed in deionised water and air dried. For electrochemical noise measurements, a Concerto multichannel potentiostat with a built in anti-aliasing filter was used. Electrochemical noise data were acquired at 1 Hz and processed by in-house software, described in detail elsewhere [20]. Electrochemical current and potential noise data were continuously recorded at 1 Hz for 11.5 days. From the time record, segments of 1024 points were extracted and, from each segment, potential and current power spectra were calculated by FFT after applying linear trend removal and Hann windowing. Smoothing of the resulting spectra was performed by the Welch method [25], with 512 points of overlap. The potential and current power spectra were used to calculate the noise impedance, the frequency of occurrence of corrosion events and the average charge associated with a single corrosion event (shot noise analysis [26–28]). For the shot noise analysis calculations, the low frequency values of current noise and potential noise were obtained by averaging the first 10 points of the low frequency region of 20 adjacent noise current and potential spectra respectively, and for the Stern-Gary coefficient, a value of 0.026 V per decade was employed [26]. High resolution scanning electron microscopy was performed using a Zeiss Ultra55 microscope.

3 Morphology of oxides obtained by the benchmark cycle

The Benchmark cycle (Table 1) involved a voltage ramp from the open circuit potential to 14 V over 5 min and subsequent potentiostatic anodizing at 14 V for 20 min in 0.4 M H_2SO_4 with the addition of 80 g L^{-1} tartaric acid at 37 °C, as prescribed by industrial specifications [4–6]. The linear relationship between applied potential and pore diameter, valid for films growing on high-purity aluminium, is valid also for oxides growing on copper-containing alloys. However, on copper-containing alloys, the porous anodic oxides display significant lateral porosity due to oxygen evolution associated with co-oxidation of copper at the alloy–film interface [5, 29]. Because the porous anodic oxide grows inward from the original alloy surface, the external regions of the oxides are generated in the early stages of the anodizing cycle, while the regions closer to the alloy interface are generated later. Thus, for the benchmark cycle, the low potentials applied during the early stages of the initial voltage ramp generate finer pores in the outer film regions compared to the pores in the inner film regions generated at a later stage of the ramp or during the final potentiostatic hold at 14 V. Figure 1a–c present the morphology of the porous oxide generated by the benchmark cycle. A porous oxide layer, approximately 3.2 μm thick (Fig. 1a), uniformly covered the macroscopic alloy surface. In Fig. 1a–c, the oxide sections appear relatively flat in some regions and more irregular in others. This is due to the specimen preparation by ultramicrotomy; at some locations, the diamond knife cuts across the oxide, producing a relatively flat section, in other regions the stresses generated during the cutting induce fracture of the oxide, generating regions that appear more irregular. Abundant lateral porosity was observed throughout the film thickness due to the oxygen evolution associated with copper co-oxidation. As expected, a relatively thin external layer ($\sim$400 nm thick, Fig. 1b) with a fine porous morphology, corresponding to the early stages of the initial voltage ramp, was revealed. However, the remaining inner oxide regions, generated later at higher potentials, displayed a relatively coarse morphology, uniform throughout the respective film thickness (Fig. 1c).

4 Primary electrolyte tuning

For the sulphuric–tartaric acid process, the relation between the applied anodizing potential and the resulting anodizing current for a given alloy is mainly determined by the concentration of the sulphuric acid (primary electrolyte), with comparatively little contribution due to the concentration of the tartaric acid [5, 9]. In order to meet the target of energy consumption reduction, both the anodizing potential and the electrolyte temperature must be reduced. Thus, the relationship between applied potential, current density and temperature for the primary electrolyte must be obtained. This was achieved by comparing the potentiodynamic anodizing response of the 0.4 M sulphuric acid electrolyte at 37 °C, representing the reference industrial condition, with the potentiodynamic responses of electrolytes with

Table 1 Anodizing parameters

Cycle ID	Electrolyte	0–14 V Sweep ($V\ s^{-1}$)	14 V Hold (s)			Duration (s)	Energy ($kW\ h\ m^{-2}$)
Benchmark	TSA	0.05	1200			1500	0.38
Cycle ID	Electrolyte	0–16 V Sweep ($V\ s^{-1}$)	16 V Hold (s)	16–6 V Sweep ($V\ s^{-1}$)	6 V Hold (s)	Duration (s)	Energy ($kW\ h\ m^{-2}$)
1-new TSA	TSA	2	60	0.1	1080	1250	0.375
2-new CeTSA	CeTSA	2	60	0.1	1080	1250	0.375
3-new CeTSA	CeTSA	2	15	0.1	1080	1200	0.265
4-new CeTSA	CeTSA	2	1	0.1	1081	1185	0.22
5-new CeTSA	CeTSA	2	1	0.1	720	825	0.178
6-new CeTSA	CeTSA	2	1	0.1	360	420	0.093

Note that benchmark cycle is performed at 37 °C, cycles 1–6 are performed at 25 °C

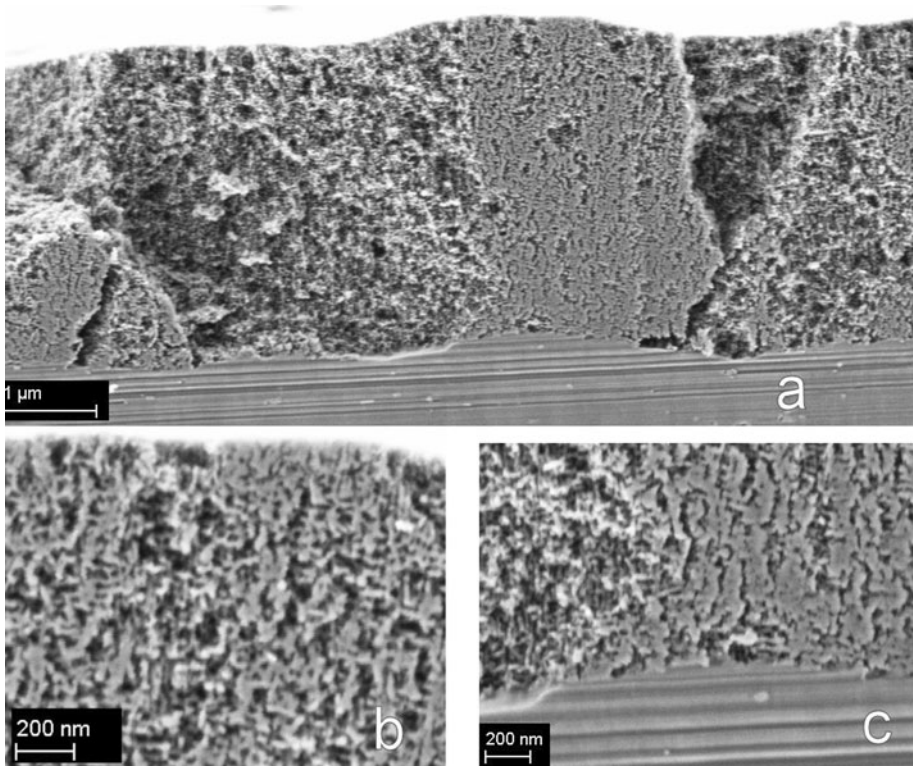

Fig. 1 **a** Scanning electron micrograph of the section of an AA2024T3 specimen anodized with the benchmark cycle (see Table 1), **b** detail of the external oxide regions and **c** detail of the alloy–film interface region

selected concentrations of electrolyte at the reduced temperature of 25 °C. Thus, potentiodynamic anodizing (2 V min^{-1}) was performed in 0.4 M H_2SO_4 at 37 °C and in 0.4, 0.8, 1.6 and 3.2 M H_2SO_4 electrolytes at 25 °C, representing new tentative electrolyte concentrations and electrolyte temperature. All the potentiodynamic responses (Fig. 2) displayed two peaks, centred at 0 and 5 volts, associated with the oxidation of Al–Mg–Cu and Al–Cu–(Fe) containing second phase particles respectively, as detailed in previous study [10, 14]. Increase of H_2SO_4 concentration increased the current density, but did not shift the characteristic potentials. On the basis of current density/potential information from Fig. 2 and from previous results [10, 14], a suitable potential for complete oxidation of second phase material and generation of fine pores is 6 V, corresponding to the end of the second peak in the curves of Fig. 2. According to the potentiodynamic curves presented, the electrolyte concentration required to achieve a current density of $\sim$10 mA cm^{-2} at 6 V, similar to the reference condition at 14 V and 37 °C, is 3.2 M H_2SO_4. Thus, in order to reduce power consumption, the anodizing potential selected to generate the majority of the inner porous oxide

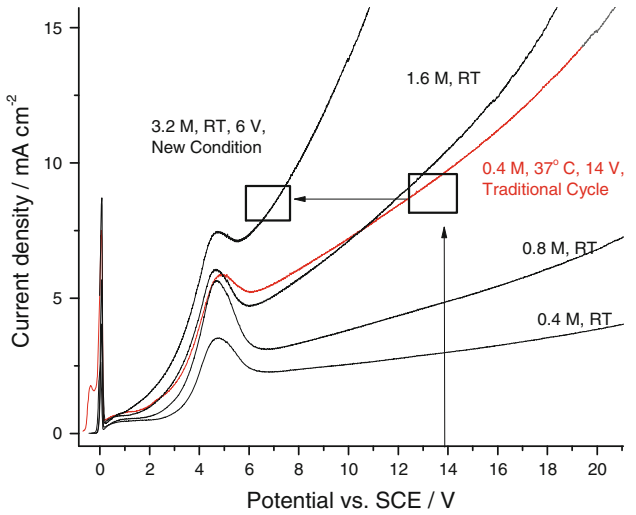

Fig. 2 Potentiodynamic response of AA2024T3 at 2 V min^{-1} in 0.4 M H_2SO_4 at 37 °C (representing the reference industrial condition) and in 0.4, 0.8, 1.6 and 3.2 M H_2SO_4 at 25 °C (representing tentative conditions)

layer and the electrolyte temperature for the new cycles are 6 V and 25 °C, respectively, both always being less than for the reference cycle (14 V and 35 °C).

5 Morphology of the oxides obtained by the new cycles

Having identified the concentration of the primary electrolyte, the electrical regime of the new anodizing cycle is carried out in 3.2 M H_2SO_4 with the addition of 80 g L^{-1} tartaric acid, with and without further addition of 1.2 g L^{-1} of cerium nitrate. The new potential-time regime is designed to generate: (i) an initial uniform barrier type oxide to prevent current concentration and localized growth during the early stages, (ii) an external oxide layer with a coarse morphology to increase adhesion with organic primers, (iii) a smooth transition layer between the external and internal regions and (iv) a relatively thick internal layer with fine morphology for enhanced corrosion resistance. Thus, recalling the linear relationship between anodizing potential and pore diameter [16, 17, 30, 31], the new anodizing cycle, (Table 1), included: (i) an initial fast voltage ramp (2 V s^{-1}) to 16 V [32], (ii) (optional) high voltage anodizing at 16 V [11, 15], (iii) a decreasing voltage ramp at 0.1 V s^{-1} [15] and (iv) low voltage anodizing at 6 V [11]. The duration of each step was tuned in order to obtain a variety of cycles, each with different energy consumption. The details regarding the duration of each anodizing step forming the new cycles are given in Table 1.

Figure 3 presents scanning electron micrographs of the sections of a porous anodic oxide generated by cycle 5-new CeTSA (Table 1). The micrographs of the oxides generated by cycle 5-new CeTSA are presented because the overall oxide thickness is similar to the thickness of the oxide generated by the benchmark cycle (3.2 μm); thus, a direct comparison between oxide morphology and protection performance is possible. The morphology of the oxides generated by cycle 5-new CeTSA can be considered representative of the morphologies generated by all the new cycles because a variation in the duration of each cycle step affects the total thickness of the oxide and the relative thickness of the outer and inner regions, but does not change their morphological characteristics. The porous anodic oxide generated by cycle 5-new CeTSA uniformly covered the macroscopic alloy surface and displayed a thickness of 3.5 μm, similar to the benchmark cycle, but the oxide morphology of the oxide was substantially different. The initial high voltage anodizing produced coarse pores in the external film regions, suitable for enhanced adhesion with organic coatings; the subsequent progressive reduction in anodizing potential gradually reduced the pore diameter, generating a very fine morphology in the inner regions of the oxide, suitable for enhanced corrosion protection. The inner layer was approximately 3 μm thick.

6 Effect of potential-time regime and electrolyte composition at constant energy consumption

In order to evaluate the effect on anticorrosion performance due to the simultaneous changes in the anodizing parameters, namely the primary electrolyte concentration, the potential-time regime and the addition of cerium nitrate, the duration of the various steps of cycles 1-new TSA and the 2-new CeTSA were tuned to consume the same energy as the benchmark cycle. Thus, it is possible to evaluate, for a given energy consumption, the effect of the morphological changes only (1-new TSA vs. benchmark) and the combined effect of the morphological changes and of the addition of cerium nitrate as inhibitor to the anodizing electrolyte (2-new CeTSa vs. 1-new TSA vs. benchmark). In Fig. 4, the potential-time regimes, the current response, the anodizing charge and the energy consumption of cycles 1-new TSA and the 2-new CeTSA are graphically compared with the benchmark cycle. Here, the anodizing charge is calculated by integrating the anodizing current over time and the energy consumed is calculated by integrating over time the product of the applied potential and the anodizing current (electric power). It is evident from Fig. 4 that, for the same energy consumed, the charge passed with the 1-new TSA and 2- new CeTSA was significantly higher compared with the benchmark cycle;

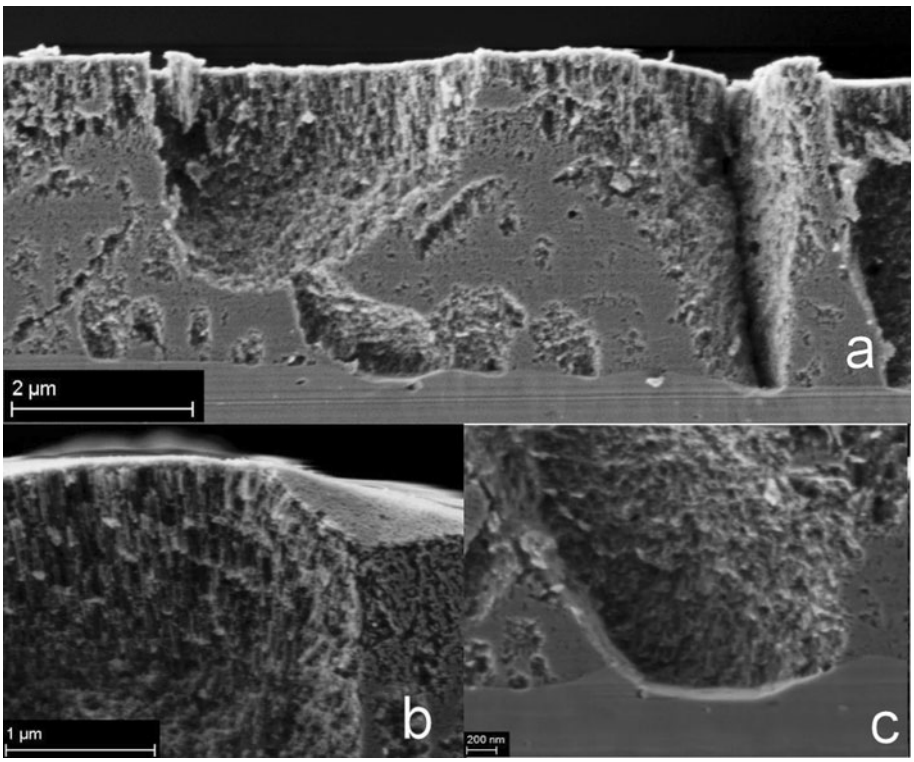

Fig. 3 **a** Scanning electron micrograph of the section of an AA2024T3 specimen anodized with the 5-new CeTsa cycle (see Table 1), **b** detail of the external oxide regions and **c** detail of the alloy–film interface region

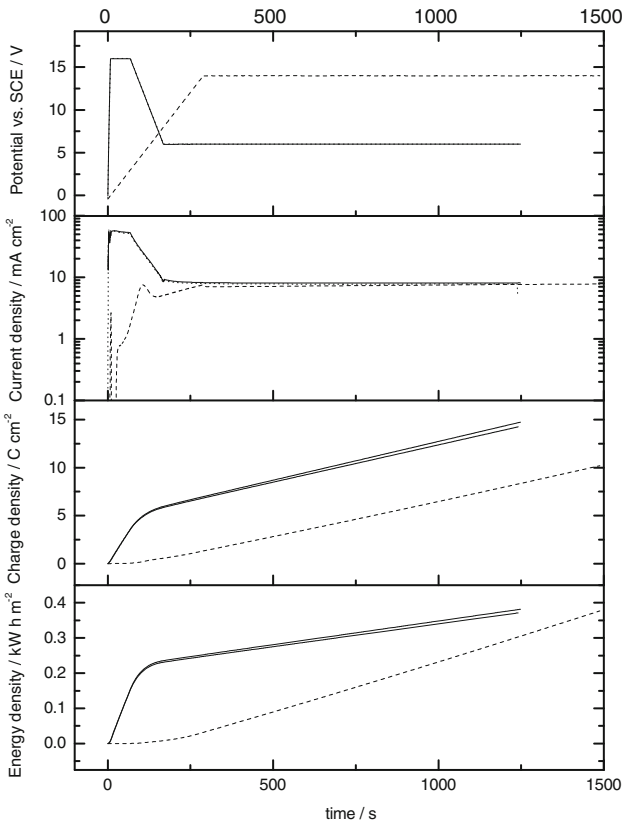

Fig. 4 Potential, current density, charge and power consumed for the benchmark cycle (*dash*) and the 1-new TSA and 2-new CeTSA (*full*)

therefore, thicker films compared with the benchmark cycle are generated.

In order to assess their anticorrosion performance after anodizing, couples of specimens having experienced the same treatment were immersed in 35 g L^{-1} NaCl and connected through a ZRA. Figure 5 presents the time evolution of the low frequency impedance, average charge for corrosion event and frequency of corrosion events calculated from the electrochemical noise data. In the low frequency impedance plot, each point is obtained by averaging the first ten points of the low frequency region of 20 adjacent noise impedance spectra. For all the specimens, during the very early stages of immersion, an initial increase of the low frequency impedance modulus was observed, possibly due to self-sealing of the pores following partial hydration of the alumina forming the pore walls. For longer immersion times, the impedance of the specimens anodized by the new TSA and the new CeTSA cycles were $\sim$100 and $\sim$1000 Ω m^{-2}, respectively, being one to two order of magnitude higher than the impedance of the specimens anodized with the traditional TSA cycle ($\sim$10 Ω m^{-2}) and suggesting significantly enhanced anticorrosion performance. The shot noise analysis indicated that larger corrosion events, $\sim$0.03 C, were associated with the specimen anodized with the benchmark cycle compared with the events proceeding on the specimens anodized with the 1-new TSA, $\sim 10^{-5}$ C, and the specimen anodized with

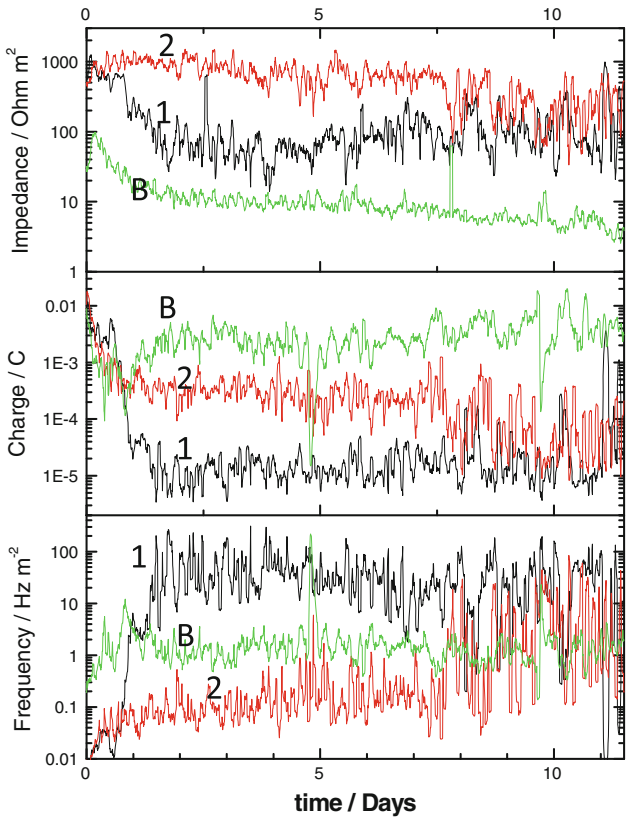

Fig. 5 Time evolution of the low frequency impedance, average charge for corrosion event and frequency of corrosion events calculated from electrochemical noise acquired in 35 g L^{-1} NaCl for the specimens anodized with the benchmark(*B*, *green*) cycle and cycles 1-new TSA (*black*) and 2-new CeTSA (*red*). (Color figure online)

the 2-new CeTSA cycle, 5×10^{-4} to 10^{-4} C. The progressive decrease of the average charge associated with a corrosion event in the case of the 2-new CeTSA anodized specimens at long immersion times may suggest active protection provided by the presence of cerium residuals. The frequency of the corrosion events was higher for the 1-new TSA anodized specimens ($\sim$100 events s^{-1} m^{-2}) than for the benchmark cycle ($\sim$1 event s^{-1} m^{-2}). The 2-new CeTSA anodized specimens initially displayed a reduced frequency of events by an order of magnitude ($\sim$0.1 events s^{-1} m^{-2}) that progressively increased with immersion time. Overall, the noise results suggest that the 2-new CeTSA anodized specimens displayed the best anticorrosion performance (high impedance, low frequency of medium magnitude corrosion events), followed by the 1-new TSA anodized specimens (medium impedance, high frequency of small corrosion events) with the benchmark cycle displaying the lowest anticorrosion performance (low impedance and high frequency of medium magnitude corrosion events).

In agreement with the electrochemical noise data, the macroscopic appearance of the specimens (Fig. 6) suggested an improved performance due to the application of the new cycles, with and without the addition of cerium nitrate. The specimens anodized according to the new cycles did not display significant macroscopic evidence of corrosion after the 11.5 days of immersion. Conversely, significant corrosion was observed on the specimens anodized using the benchmark cycle (Fig. 6).

7 Low energy anodizing cycles

Based on the previous results, a series of similar anodizing cycles were investigated by tuning the duration of each step, e.g. initial high voltage hold and duration of the final low-potential hold in the CeTSA electrolyte (Table 1, cycles 3–6-new CeTSA). The values of energy consumed by cycles 3, 4, 5 and 6-new CeTSA were respectively 30, 42, 52 and 75% less than the energy consumed by the benchmark cycle and by cycles 1-new TSA and 2-new CeTSA.

The anticorrosion performance of each cycle was evaluated by electrochemical noise using the procedure previously described (Fig. 7). For cycles 3, 4 and 5-new CeTSA, the low frequency impedance values calculated from the electrochemical noise signals progressively decreased from 1000 to about 100 Ω m^2 during immersion, revealing similar behaviour to that previously revealed for cycles 2 and 3 (new TSA and new CeTSA). Such behaviour indicates satisfactory corrosion resistance. However, the specimens anodized under cycle 5 displayed a slightly faster decrease in the reduction of the noise impedance, achieving a value of 100 Ω m^2 after only 2 days of immersion. Conversely, the specimens anodized under cycle 6 displayed one order of magnitude lower values of noise impedance (100–10 Ω m^2), comparable with those revealed for the benchmark cycle. Shot noise analysis indicated that the average charge for a corrosion event was similar for all the specimens in the early stages of immersion, $\sim 10^{-3}$ C, and progressively decreased by about one order of magnitude for the specimens anodized under cycles 3, 4 and 5-new CeTSA. The specimens anodized under cycle 6 did not experience such a decrease. The frequency of corrosion events increased from $\sim$0.01 and $\sim$0.1 events s^{-1} m^{-2} for specimens anodized under cycles 3, 4, 5 and under cycle 6, respectively to a final value of $\sim$10 events s^{-1} m^{-2} for all the specimens. In summary, the electrochemical noise data suggest that the specimens anodized under cycles 3 and 4 displayed a very good corrosion resistance (high impedance, low frequency of medium magnitude corrosion events), the specimens anodized under cycle 5 displayed an intermediate behaviour (relatively fast reduction of impedance, low frequency of medium magnitude corrosion events) and the specimen anodized under cycle 6 displayed a relatively poor corrosion resistance.

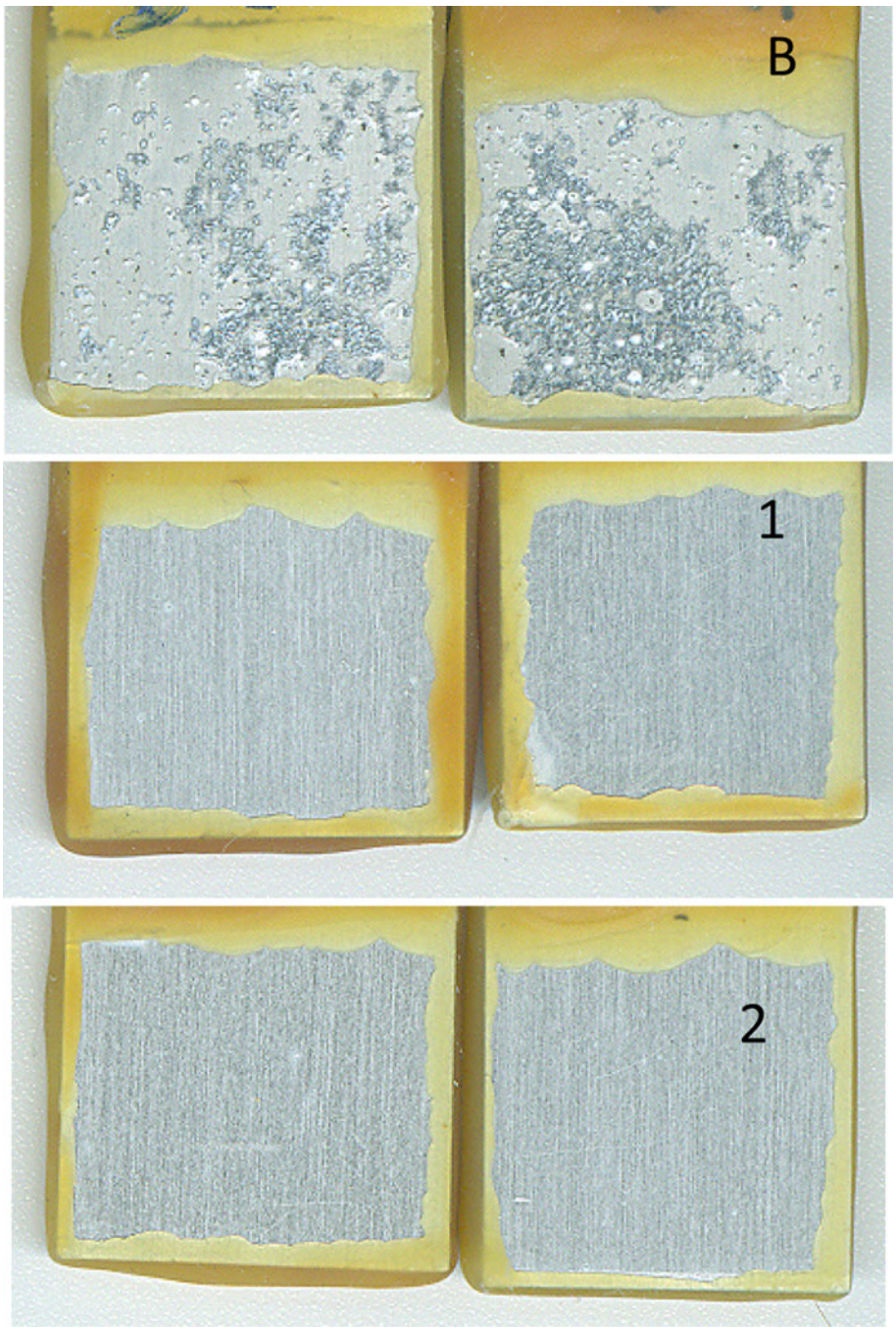

Fig. 6 Specimens surface after immersion in 35 g L^{-1} NaCl for 11.5 days; B-benchmark anodizing cycle, 1-new TSA cycle and 2-new CeTSA cycle

The surface appearance of the specimens after the 11.5 days of immersion (Fig. 8) confirmed the electrochemical noise results; the specimens anodized under cycle 3 displayed no visible signs of corrosion, while some isolated pits were evident on the specimens anodized under cycle 4 and 5. Finally, the specimens anodized under cycle 6 displayed corrosion of comparable extent to that observed on the specimen anodized with the benchmark cycle. In summary, all the specimens anodized with the new cycles, except for the specimens anodized under cycle 6, displayed a better anticorrosion performance than the specimens anodized with the benchmark cycle (Fig. 9).

8 Scanning electron microscopy observation after immersion

Having identified cycle 5-new CeTSA as the preferred low energy consuming cycle (−52% energy and −42% process time) that is capable of providing enhanced corrosion

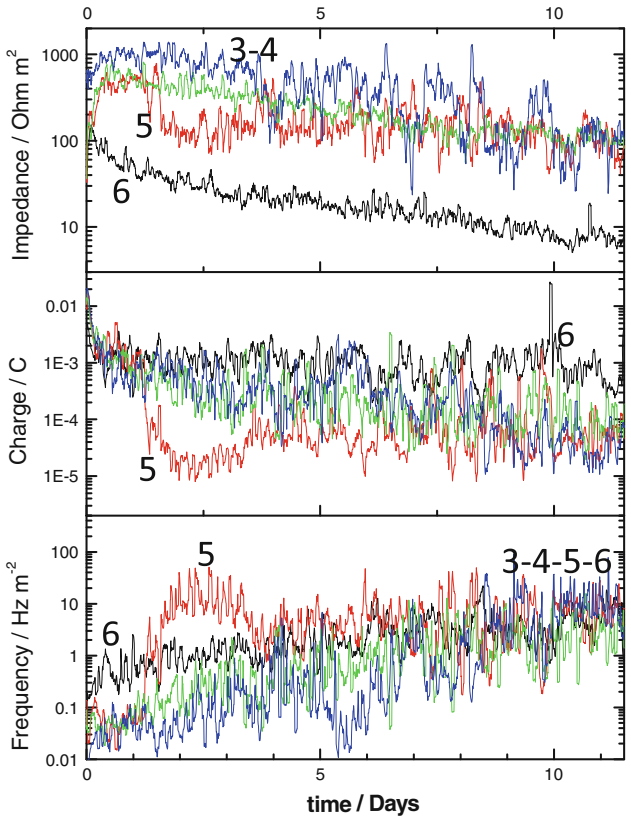

Fig. 7 Time evolution of the low frequency impedance, average charge for corrosion event and frequency of corrosion events calculated from electrochemical noise acquired in 35 g L^{-1} NaCl for the specimens anodized under cycles 3 (*green*), 4 (*blue*), 5 (*red*) and 6 (*black*). (Color figure online)

protection compared with the benchmark cycle, scanning electron microscopy was undertaken on sections of both porous anodic oxides after immersion for 11.5 days in 35 g L^{-1} NaCl. After corrosion testing, the specimen anodized with the benchmark cycle displayed a two-layer film morphology (Fig. 10a); close to the alloy interface, a residual layer of porous anodic oxide, was observed (Fig. 10b), covered by a corrosion product layer of variable thickness (Fig. 10c), depending on the location examined. Close to a corrosion site, on the left of Fig. 10a, the residual porous anodic oxide was thinner compared to locations far from the corrosion site. Overall, a significant deterioration of the oxide was observed on all the macroscopic surface, due to significant corrosion. Conversely, the specimen produced with cycle 5-new CeTSA, did not display a layer of corrosion products, and the integrity of the anodic oxide was generally maintained, although at some location the oxide was thinner (Fig. 11a). In general, the original porous structure could be observed throughout the thickness of the oxide, with the larger pores still evident in the outer regions (Fig. 11b) and the finer pores unchanged in the inner regions (Fig. 11c).

9 Mechanisms of protection/degradation

The precise mechanism leading to deterioration of the porous anodic oxide and corrosion propagation in the case of the specimen anodized with the benchmark cycle requires further study and is presently under investigation. From this study, however, the progressively thinner oxide at locations closer to a corrosion site (Fig. 10a) suggests that generalized porous anodic oxide degradation is mainly due to pH changes following a sustained and localized anodic or cathodic reaction. In proximity of an anodic site, the lower pH promotes the dissolution/hydration of the surrounding porous anodic oxide that becomes thinner, with abundant precipitation of hydrated products. Importantly, a similar oxide degradation effect is expected at active cathodic sites, where the pH increases due to oxygen reduction may promote similar oxide dissolution/hydration. It is of some interest to speculate if, during the stage of corrosion initiation, the critical step to trigger oxide degradation, and subsequent exposure of large areas of unprotected alloy, is the pH decrease in proximity of active anodic sites or the pH increase in proximity of the cathodic sites or a combination of both. As previously explained, for the AA2024T3 alloy, a minimum potential of 6 V is required to completely oxidize the copper-containing second phase material, so that the presence of cathodic sites of the surface after anodizing is minimized. If a lower potential is applied, the alloy matrix anodizes preferentially compared with the second phase material [10, 12, 14] and an increase in the relative area of the cathodic sites is observed with increasing anodizing time, with detrimental effects on the performance [11]. However, for a given alloy, even after anodizing at sufficiently high potentials, some partially unoxidized second phase particle, covered by a highly flawed oxide due to the high yields of alloying elements, must be present on the surface. This is simply due to the fact that the alloy interface recedes during anodizing, and new second phase particles that were previously buried in the bulk alloy are continuously exposed to the anodizing electrolyte. Thus, when anodizing is terminated, some particles are only partially oxidized and remain as residual cathodic sites on the anodized surface. Considering that this is in essence a geometrical effect due to the receding macroscopic interface, it is expected that under conditions favourable for particle oxidation (i.e. over 6 V for AA2024T3), the anodizing potential does not affect significantly their distribution and, thus, the number and size of available cathodic sites after anodizing. Consequently, the finer or coarser oxide morphology associated with lower or higher anodizing potential respectively must predominantly affect the protection properties over the anodic alloy matrix. Evidence form previous study, showing that the corrosion performance (for a given

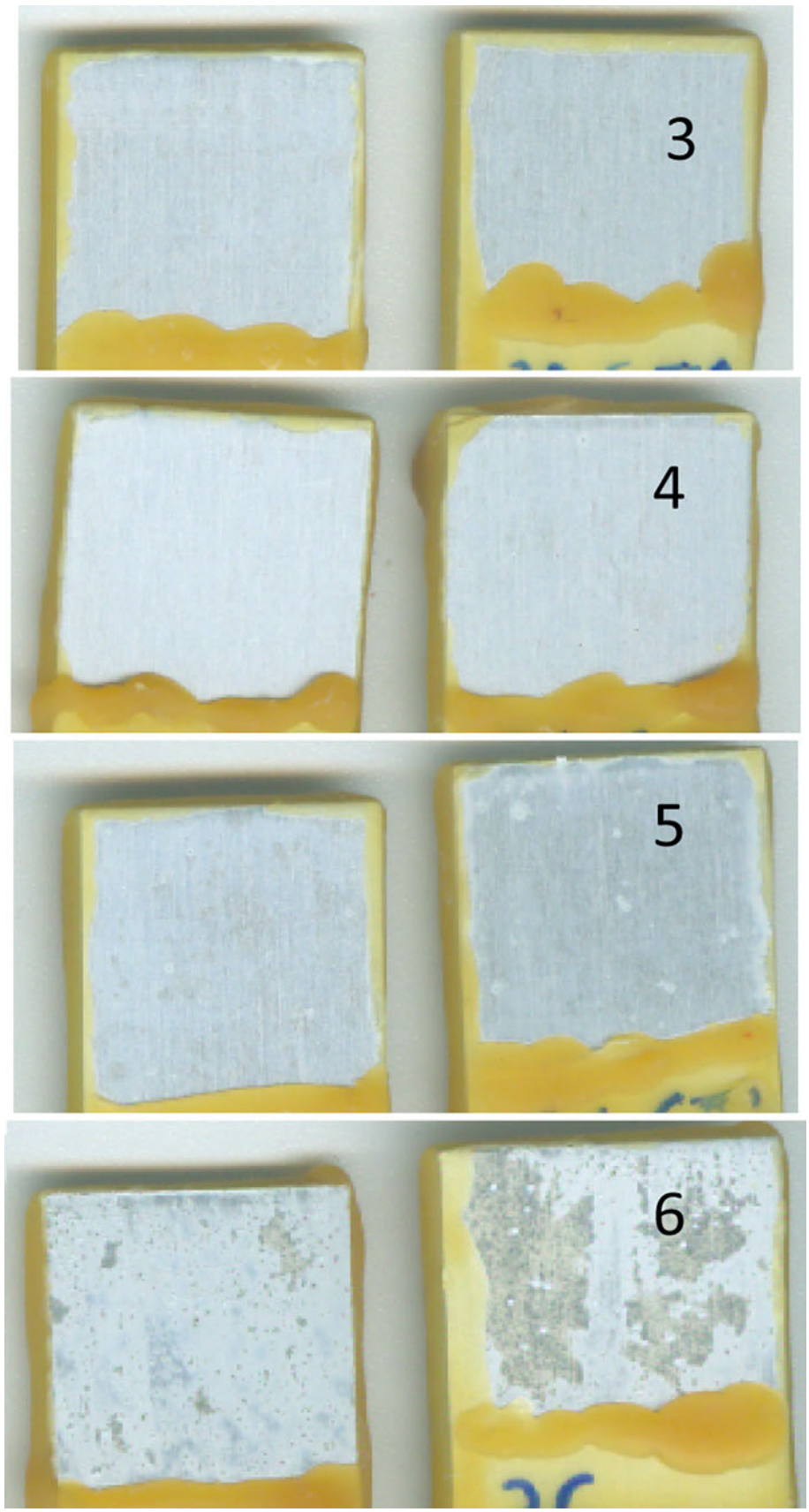

Fig. 8 Specimens surface after immersion in 35 g L^{-1} NaCl for 11.5 days; numbers indicate the new CeTSA anodizing cycle as from Table 1

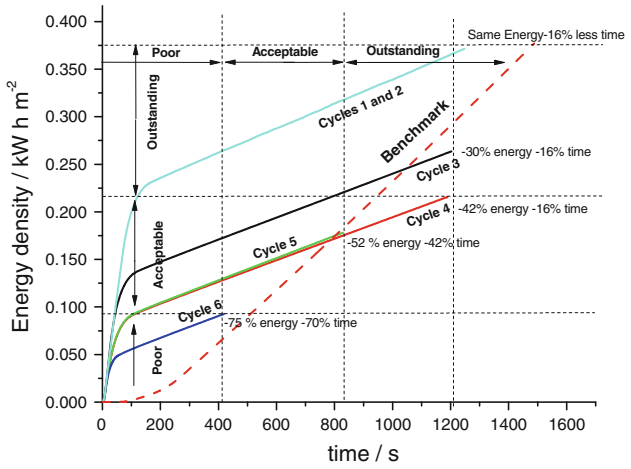

Fig. 9 Time evolution of the energy consumed (time integral of the product between applied potential and anodizing current) for all the anodizing cycles described in Table 1 and resulting energy–time-performance map for the new CeTSA process

electrolyte and a given charge/oxide thickness) increases with decreasing anodizing potential, until the minimum potential required to oxidize the second phase material [11], are supported here by the comparison between the 1-new TSA cycle and the benchmark cycle, obtained in similar electrolytes. Finer pores provide a better protection to the anodic alloy matrix, limiting the exchange of aggressive species (i.e. Cl^-) and, due to the reduced size, might partially self-seal by hydration without disruption of the original morphology, producing an effective anodic barrier. Thus, for specimens with comparable cathodic activity, the capability of the oxide to obstacle the occurrence of anodic events, and associated local acidification, is important in determining the overall anticorrosion behaviour. Proceeding further, the comparison of the performance of the oxides generated in identical conditions except for the absence or presence of cerium nitrate in the anodizing electrolyte, namely the 1-new TSA and the 2-new CeTSA, also enables evaluation of the role of active cathodic sites on the process of corrosion initiation. Cerium nitrate is an effective cathodic inhibitor, but has little effect on the anodic kinetics [20]. Thus, the enhanced anticorrosion performance of the anodic oxides generated in the presence of cerium nitrate suggests that the beneficial effect of de-activation of the residual active cathodic sites acts synergistically with the effective anodic barrier provided by the finer pores. The cathodic inhibition effect not only prevents corrosion by reducing the rate of oxygen reduction, but also prevents the degradation of the oxide in the surrounding region by limiting or avoiding the pH increase. Thus, in the absence of cathodic inhibitor, a sustained cathodic reaction produces alkalinization and progressive deterioration of the anodic oxide in the vicinity of the cathodic site, with subsequent exposure of unprotected metal. Conversely, the presence of a cathodic

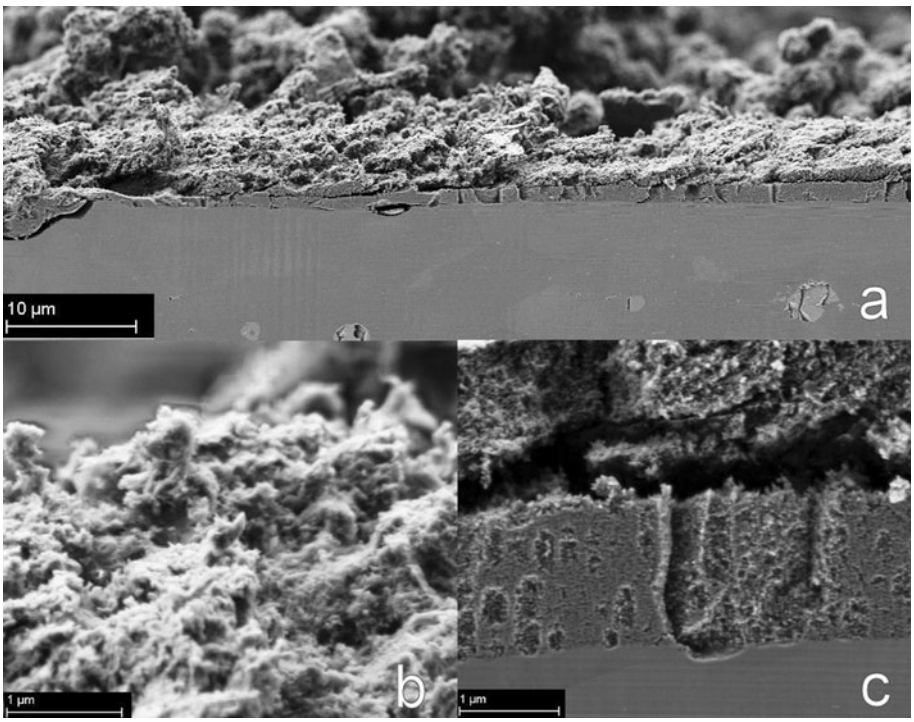

Fig. 10 **a** Scanning electron micrograph of the section of an AA2024T3 specimen anodized with the benchmark cycle (see Table 1) after immersion for 11.5 days in 35 g L^{-1} NaCl, **b** detail of the external regions (corrosion products) and **c** detail of the alloy–anodic oxide film interface region

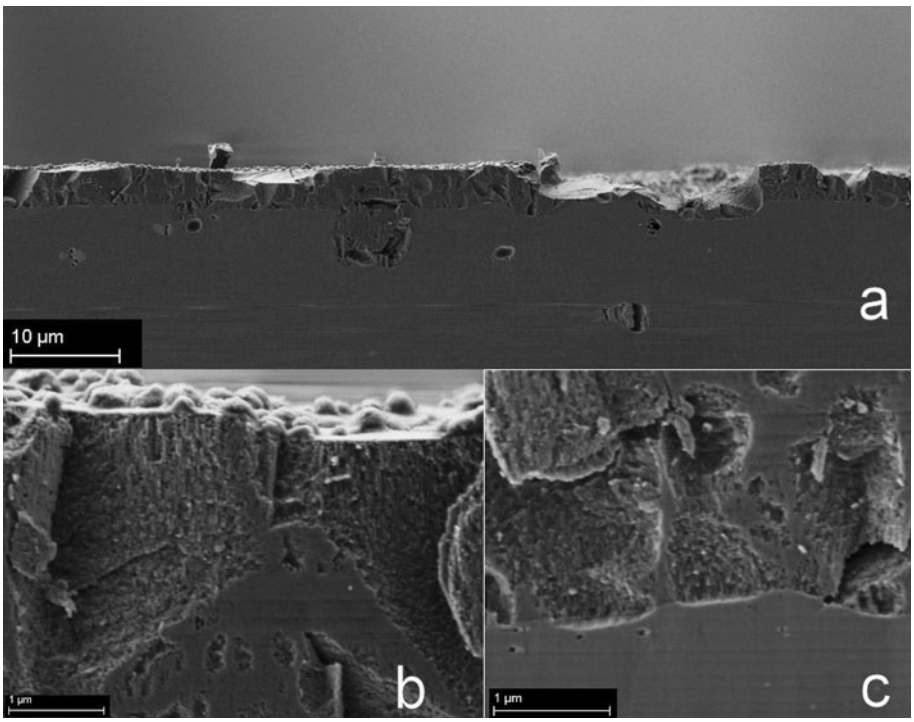

Fig. 11 **a** Scanning electron micrograph of the section of an AA2024T3 specimen anodized with the 5-newCeTSA cycle (see Table 1) after immersion for 11.5 days in 35 g L^{-1} NaCl, **b** detail of the external anodic oxide regions and **c** detail of the alloy–anodic oxide film interface region

inhibitor limits the alkalinization and, consequently, the surrounding porous anodic oxide is preserved, protecting the underlying metal.

10 Summary

A methodology for the development and validation of a low energy anodizing cycle has been developed and applied to reduce the energy consumption associated with protective anodizing cycles for aerospace components. It has been shown that by examination of the potentiodynamic anodizing response and by tailoring of the oxide morphology, it is possible to reduce the anodizing temperature and the anodizing potential, without compromising the anticorrosion performance or extending the duration of the anodizing cycle. With this approach, the electrical energy required to complete the anodizing cycle can be reduced by up to 52% and the process time reduced by 42% compared with the reference anodizing cycle with importantly enhanced anticorrosion performance. The new low energy CeTSA cycles exploit the beneficial effects of anodic barrier provided by the very fine porous oxide morphology combined with the cathodic inhibition provided by the addition of cerium nitrate to the anodizing electrolyte. Further, it is also suggested that the reduced alkalinization at cathodic sites due to the cathodic inhibition of cerium nitrate has a synergistic beneficial effect; it avoids disruption of the anodic oxide in the proximity of the cathodic sites due to alkalinization, preventing exposure of additional cathodic sites.

Acknowledgements The authors acknowledge the financial support provided by the Engineering and Physical Sciences Research Council Programme Grant, LATEST2.

References

1. Paez MA, Zagal JH, Bustos O et al (1997) Electrochim Acta 42:3453
2. Morlidge JR, Skeldon P, Thompson GE et al (1999) Electrochim Acta 44:2423
3. Garcia-Vergara SJ, Habazaki H, Skeldon P et al. (2007) Nanotechnology 18:415605
4. Dattilo A, Tamiro S, Romano C (2002) EU Patent EU1233084
5. Iglesias-Rubianes L, Garcia-Vergara SJ, Skeldon P et al (2007) Electrochim Acta 52:7148
6. García-Rubio M, Ocón P, Climent-Font A et al (2009) Corros Sci 51:2034
7. García-Rubio M, Ocón P, Curioni M et al (2010) Corros Sci 52:2219
8. Curioni M, Skeldon P, Koroleva E et al (2009) J Electrochem Soc 156:C147
9. Boisier G, Pebere N, Druez C et al (2008) J Electrochem Soc 155:C521
10. Curioni M, Saenz De Miera M, Skeldon P et al (2008) J Electrochem Soc 155:C387
11. Curioni M, Skeldon P, Thompson GE et al (2008) ECS Trans 13:41
12. Saenz De Miera M, Curioni M, Skeldon P et al (2010) Surf Interface Anal 42:241
13. Saenz de Miera M, Curioni M, Skeldon P et al (2010) Corros Sci 52:2489

14. Saenz de Miera M, Curioni M, Skeldon P et al (2008) Corros Sci 50:3410
15. Curioni M, Skeldon P, Thompson GE et al (2008) Adv Mat Res 38:48
16. Wood GC, O'Sullivan JP (1970) Electrochim Acta 15:1865
17. O'Sullivan JP, Wood GC (1970) Proc R Soc Lond Ser A 317:511
18. Moutarlier V, Gigandet MP, Ricq L et al (2001) Appl Surf Sci 183:1
19. Moutarlier V, Gigandet MP, Normand B et al (2005) Corros Sci 47:937
20. Rosero-Navarro NC, Curioni M, Bingham R et al (2010) Corros Sci 52:3356
21. Hinton BRW, Arnott DR, Ryan NE (1986) Mater Forum 9:162
22. Gorman JD, Johnson ST, Johnston PN et al (1996) Corros Sci 38:1977
23. Hughes AE, Gorman JD, Paterson PJK (1996) Corros Sci 38: 1957
24. Wan J, Thompson GE, Lu KQ et al. (1997) Journal De Physique IV: JP 7
25. Welch PD (1967) IEEE Trans Audio Electroac AU-15:70
26. Sanchez-Amaya JM, Cottis RA, Botana FJ (2005) Corros Sci 47:3280
27. Cottis RA (2006) Russ J Electrochem 42:497
28. Kuznetsov AM (2008) Russ J Electrochem 44:1327
29. Curioni M, Roeth F, Garcia-Vergara SJ et al (2010) Surf Interface Anal 42:234
30. Thompson GE, Furneaux RC, Goode JS et al (1978) Trans Inst Met Fin 56:159
31. Curioni M, Koroleva EV, Skeldon P et al. (2010) Electrochim Acta 55:7044
32. Curioni M, Skeldon P, Thompson GE (2009) J Electrochem Soc 156:C407